Enhanced Stability and Activity of Pt–Y Alloy Catalysts for Electrocatalytic Oxygen Reduction

Sung Jong Yoo,[a] Soo-Kil Kim,[a] Tae-Yeol Jeon,[b] Seung Jun Hwang,[a] June-Gunn Lee,[c] Seung-Cheol Lee,[c] Kug-Seung Lee,[a] Yong-Hun Cho,[d] Yung-Eun Sung[b] and Tae-Hoon Lim[a]*

[a]Fuel Cell Center, Korea Institute of Science and Technology, 39-1 Hawolgok-dong, Seoul 136-791, Korea

[b]World Class University Program of Chemical Convergence for Energy & Environment, School of Chemical and Biological Engineering, Seoul National University, 56-1 Shinlimdong, Seoul 151-742, Korea

[c]Computational Science Center, Korea Institute of Science and Technology, 39-1 Hawolgok-dong, Seoul 136-791, Korea.

[d]School of Advanced Materials Engineering, Kookmin University, 861-1 Jeongneung-dong, Seoul 136-702, Korea

*Address correspondence to this author. Tel: 82-2-958-5201, Fax: 82-2-958-5199, E-mail: thlim@kist.re.kr

Contents

1. **Geometric surface of the Pt-Y alloy electrodes**
2. **Confirmation of the electrochemically active surface area**
3. **Bulk composition analysis**
4. **Sample perpetration and electrochemical characterization using a rotating disk electrode**
5. **Synchrotron X-ray diffraction**
6. **Valence band spectra using synchrotron high-resolution X-ray photoelectron spectroscopy**
7. **Synchrotron X-ray absorption fine structure spectroscopy**
8. **Synchrotron extended X-ray absorption fine structure spectroscopy**
9. **Computation method using DFT calculation**
10. **Fuel cell test of the Pt-Y alloy electrocatalysts fabricated by using sputter technique**
11. **Y 3d peaks using synchrotron high-resolution X-ray photoelectron spectroscopy**
12. **References**

1. Geometric surface of the Pt-Y alloy electrodes

First of all, we have studied the geometric surface of the electrode fabricated by sputtering process, because the geometric surface could make the evaluation of the results difficult. So before the oxygen reduction reaction (ORR) was evaluated on the Pt-Y electrodes, we have investigated the sputtering power and deposition pressure-dependent surface morphology and structural behavior of sputter-deposited Pt-Y electrodes on silicon (Si) substrates or glass carbon (GC).

The thicknesses for the Pt-Y electrodes deposited at various sputtering powers were tabulated in Table S1, which shows deposition rate increases linearly with the sputtering power.

We attribute this dependence relationship to the determinacy of sputter deposition rate on the Ar ion flux and its average kinetic energy upon striking the target. The high Ar ion flux generally results in substantial ion bombardment on the target while the high kinetic energy of these ions increases the probability that the impacts of incident ions will eject target atoms. These two mechanisms are proportional to sputtering power, and hence contribute to the increase of the sputter deposition rate. Similar dependence relationship between deposition rate and sputtering power was reported [1].

Figure S1(a) demonstrates the qualitative dependence of the Pt-Y electrodes roughness on the sputtering power, in which the roughness increases with increasing sputtering power. For the Pt-Y electrodes deposited at sputtering power of 100, 125, 150, 200 and 300 W, the corresponding roughness are 0.31, 0.49, 1.01, 4.33 and 8.12 nm, respectively. The roughness increases with sputtering power. The possible factors contribute to the decrease in film roughness at lower sputtering power are lower thickness due to the lower deposition rate achieved with lower sputtering power [2], and decrease of surface and bulk diffusion (surface mobility) due to the low ad-atom energy. To demonstrate this, Figure S1(b) illustrates the plots of roughness versus thickness for Pt-Y electrodes deposited at varied sputtering power (ranging from 100 to 300 W). This curve shows that in general those Pt-Y electrodes deposited at lower sputtering power exhibit lower roughness compared to Pt-Y electrodes of similar thickness but grown at higher sputtering power. This corroborates our conclusion for which the lower sputtering power with lower surface diffusion and ad-atom mobility improves the roughness of the Pt-Y electrodes.

Table S1. *Deposition parameters and the thicknesses for the sputter-deposited Pt-Y electrodes.*

Target	Pure Pt, pure Y
Substrate	Si and GC
Target-substrate distance	25 cm
Substrate temperature	Room temperature
Base pressure	< 5 x 10^{-7} torr

Sample (thickness)	**Deposition time (min)**	**Deposition pressure (10^{-3} torr)**	**Sputter power (W)**
			Total power
S-Pt-Y (90 nm)	10	10	100
S-Pt-Y (200 nm)	10	10	125
S-Pt-Y (330 nm)	10	10	150
S-Pt-Y (460 nm)	10	10	200
S-Pt-Y (640 nm)	10	10	300
P-Pt-Y (95 nm)	10	1	100
P-Pt-Y (103 nm)	10	5	100
P-Pt-Y (108 nm)	10	10	100
P-Pt-Y (113 nm)	10	20	100
P-Pt-Y (116 nm)	10	30	100

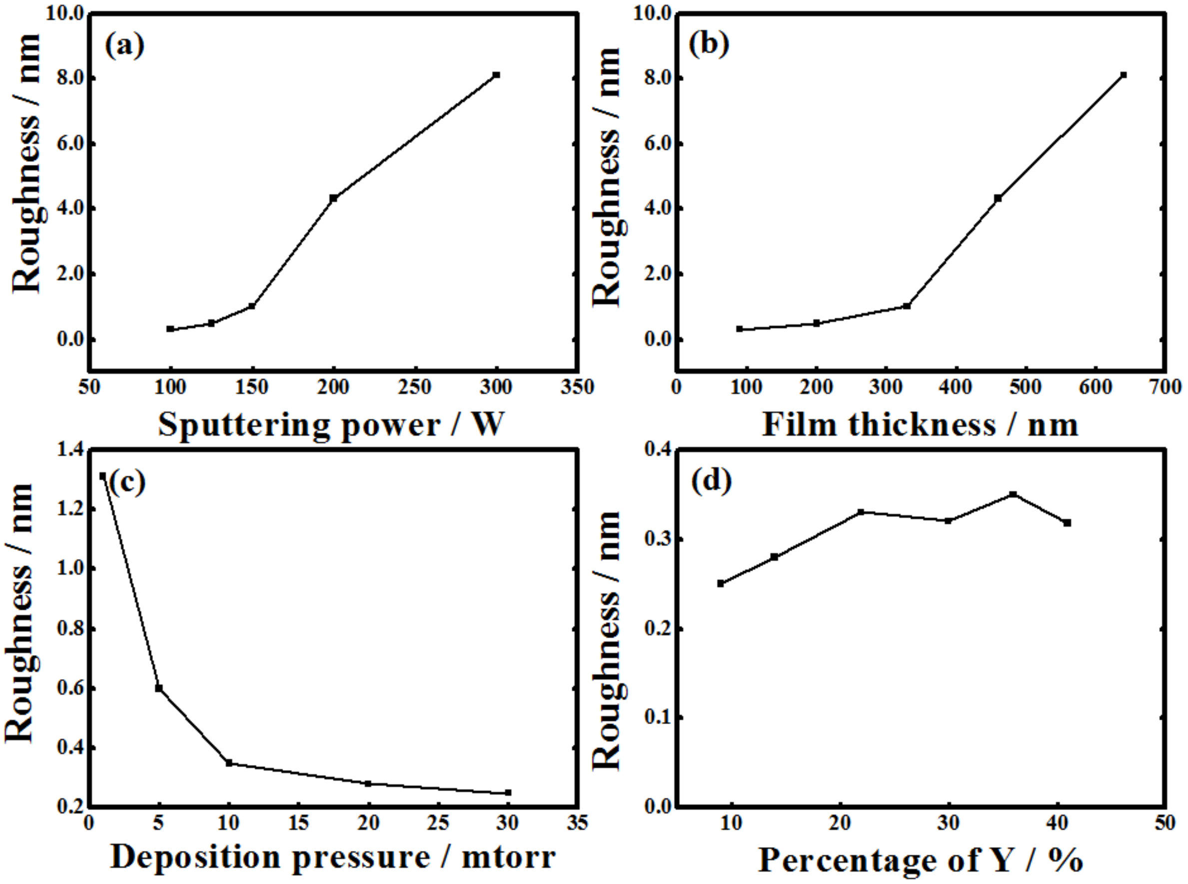

Figure S1. *(a) Dependence of the roughness on the sputtering power. (b) Roughness vs. film thickness varied sputtering power. (c) Deposition of the roughness on the deposition pressure. (d) The Roughness of* $Pt_{91}Y_{9}$, $Pt_{86}Y_{14}$, $Pt_{78}Y_{22}$, $Pt_{70}Y_{30}$, $Pt_{64}Y_{36}$, *and* $Pt_{59}Y_{41}$*electrodes.*

The plot of Pt-Y electrodes roughness versus deposition pressure at 100 W was illustrated in Figure S1(c), which shows that the Pt-Y electrodes roughness decreases exponentially with the deposition pressure. At 1 mTorr, the roughness is 1.31 nm. At elevated deposition pressure of 5, 10, 20 and 30 mTorr, the roughnesses are 0.60, 0.35, 0.28, and 0.25 nm, respectively. The Pt-Y electrodes roughness was decreased with the increase in deposition pressure ranging from 1 to 30 mTorr as shown in Figure S1(c). Although the Pt-Y electrodes deposited at low deposition pressure show the high-quality crystallinity, its high roughness have the problem to measure the ORR because of the geometric effect. So we optimized the condition of sputter process for the reasonable ORR measurement. The real kinetic current density on Pt electrode promoted Y would be affected by the geometric effect, but we believed that the use of the kinetic current density measured in our electrodes was reasonable to elucidate the phenomena of the Y-alloying effect, due to the similar smooth roughness (< 0.33 nm) of all Pt-Y electrodes, as shown in Figure S1(d) and S2.

We conclude that by proper control of the sputtering power and deposition pressure, the roughness of the real surface of the sputter-deposited Pt-Y electrodes on Si or GC could be minimized. We believe that this could allow the evaluation of the ORR performance of the Pt-Y electrodes, which were fabricated by sputter process in the optimum condition.

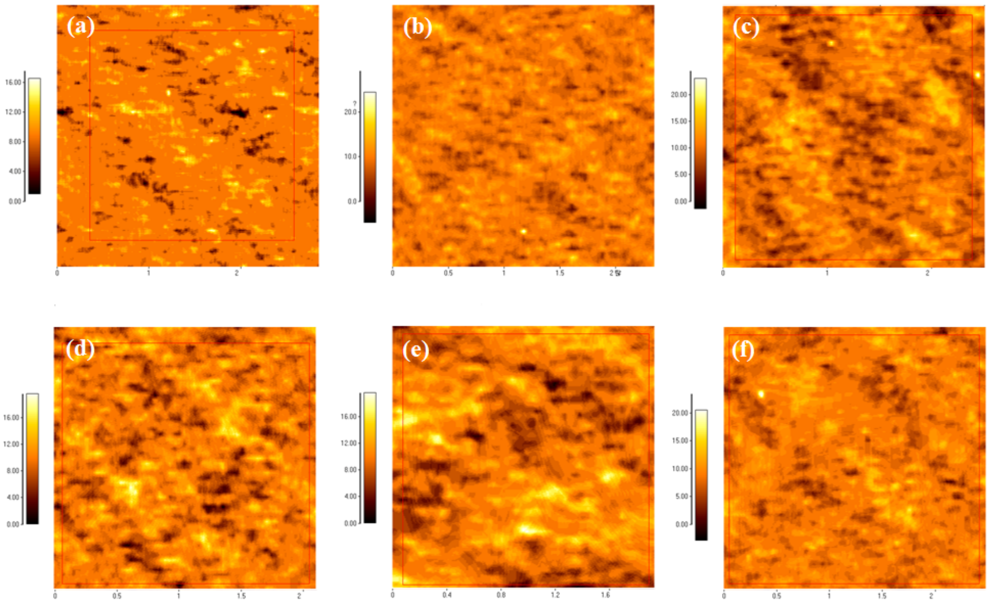

***Figure S2**. AFM topography images of (a) $Pt_{91}Y_9$, (b) $Pt_{86}Y_{14}$, (c) $Pt_{78}Y_{22}$, (d) $Pt_{70}Y_{30}$, (e) $Pt_{64}Y_{36}$, and (f) $Pt_{59}Y_{41}$ electrodes deposited at 10 mtorr and 100 W on Si substrate. The surface morphology of the films was observed by atomic force microscopy (AFM; XE-100 SPM system, PSIA Co., Korea).*

2. Confirmation of the electrochemically active surface area

The CO-stripping measurement was used to estimate the real surface area of the electrodes, following the procedures. The 0.1 M $HClO_4$ solution was purged with Ar gas for 30 min prior to electrochemical measurements. For CO-stripping measurements, pure CO was bubbled into the electrolyte under potential control at 0.1 V vs. NHE for 30 min. Then, the electrolyte was purged for 30 min with Ar gas, while keeping the electrode potential at 0.1 V vs. NHE to eliminate the dissolved CO in the electrolyte. The first anodic scan (scan speed: 10 mV s^{-1}) was performed to electro-oxidize the adsorbed CO and the subsequent voltammetries in order to verify the completeness of the CO oxidation. Assuming that each Pt surface atom is covered by a single adsorbed CO molecule, the charge for electro-desorption of CO should be 420 μC cm^{-2}. Figure S3 shows the voltammograms of Pt and $Pt_{70}Y_{30}$ in the presence and the absence of CO. The integrated CO stripping charge for all voltammograms came to 84 ± 5 μC, irrespective of the electrode composition. This suggests that the geometric (0.196 cm^2) and real surface areas are almost equal (about 0.2 ± 0.01 cm^2). This result is in good agreement with AFM data.

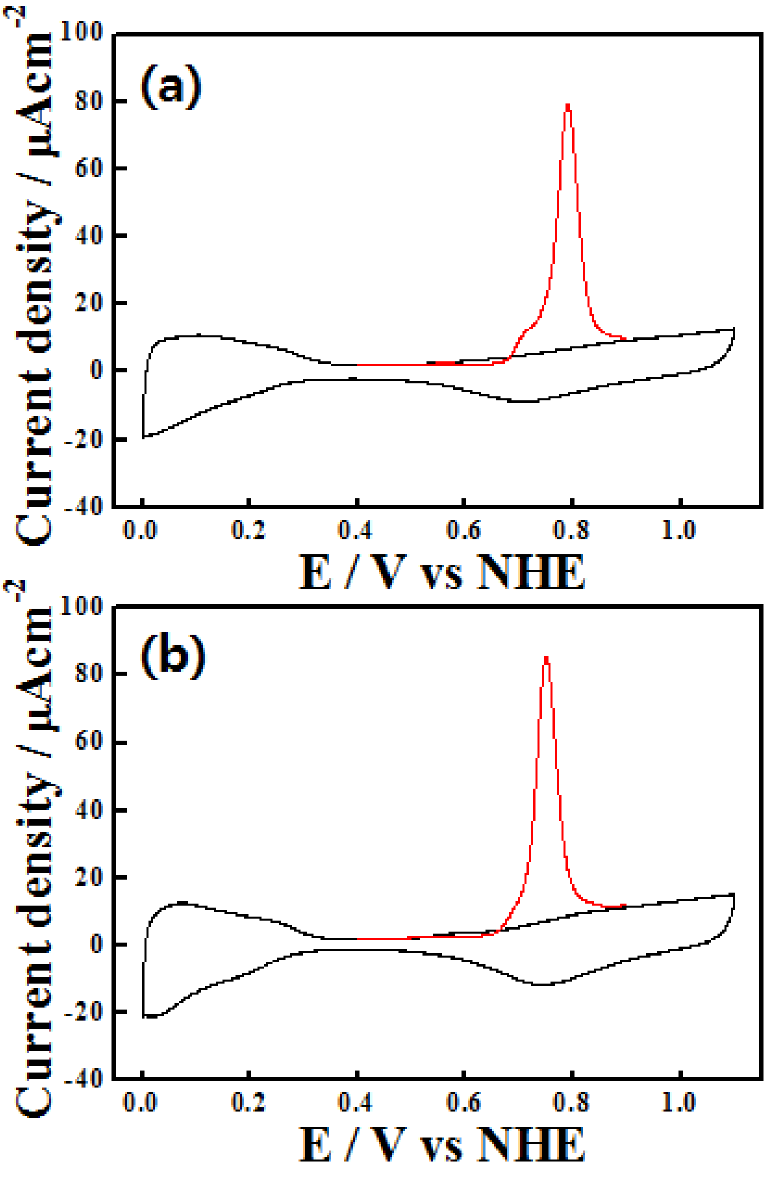

***Figure S3**. CO-stripping data of (a) Pt and (b) $Pt_{70}Y_{30}$.*

3. Bulk composition analysis

Before examining the catalytic activity and stability, the electrodes were characterized by Auger electron spectroscopy (AES) in a scanning Auger nanoprobe (ULVAC PHI-700). The sample surface was sputtered for 5 s before AES measurements. The AES spectra were recorded using a 3 keV accelerating voltage with a spot size of 150 µm, recorded over the range 20 to 2420 eV. The chamber was held at a base pressure below 5×10^{-10} Torr.

Figure S3 shows the Auger spectra for the Pt-Y electrodes, respectively. Evidently all the peaks correspond to those characteristic of Pt and Y. According to these spectra, in the near surface region the compositions of the Pt-Y electrodes were ~91% Pt and ~9 % Y, ~86% Pt and ~14 % Y, ~78% Pt and ~22 % Y, ~70 % Pt and ~30 % Y, ~64 % Pt and ~36 % Y, and ~59 % Pt and ~41 % Y.

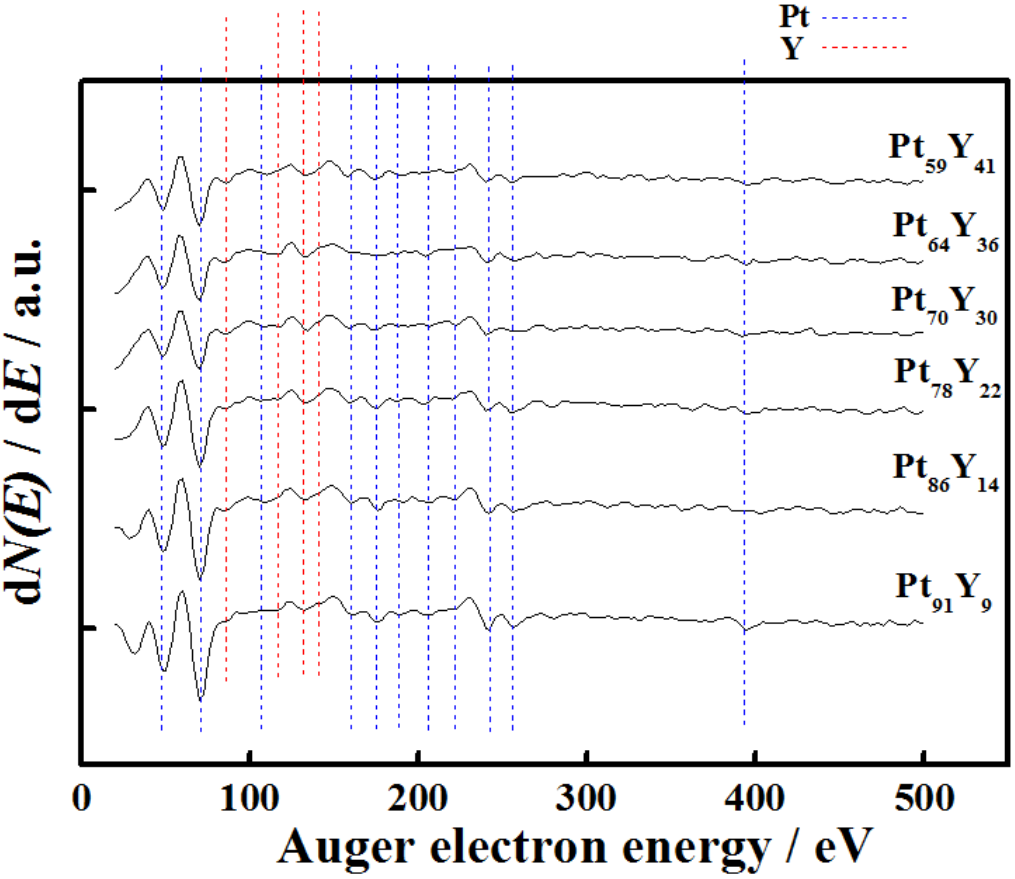

Figure S4. *AES spectra of Pt-Y electrodes.*

4. Sample perpetration and electrochemical characterization using a rotating disk electrode

Pt–Y alloy electrodes were grown using a radio-frequency (RF) magnetron co-sputtering system comprising a dual sputtering gun. Si (100) and glassy carbon were used as substrates to characterize the structural and electrochemical properties, respectively. Co-sputtering was performed under inert Ar gas at a flow rate of 26 sccm at room temperature for 10 min, and this produced films with a thickness of approximately 100 nm. In order to fabricate Pt–Y thin-film electrodes with various compositions, the guns with the metal targets in the RF magnetron sputtering system were controlled as a function of the RF power. As the RF power of the Y target gun was increased at a fixed RF power of the Pt gun, the Y concentration was varied from 0% to 41%.

An AutoLab PGSTAT20 potentiostat and a rotating disk electrode (RDE) system (Ecochemie) with a conventional three-electrode configuration were used for all the electrochemical measurements. All the electrochemical measurements, except for the ORR with the RDE configuration, were performed in an Ar-purged 0.1 M $HClO_4$ solution. For the ORR experiment, 99.99% oxygen gas was bubbled into the electrolyte for 60 min before each measurement. A catalyst-coated glassy carbon electrode with a diameter of 5 mm was used as the working electrode. Before each measurement, the glassy carbon electrode was polished with a 0.05-μm alumina paste followed by washing with distilled (DI) water in an ultrasonic bath. A saturated calomel electrode (SCE) with 3 M KCl (Gamry) and a glassy carbon rod were used as the reference and counter electrodes, respectively. However, in this paper, all the potentials reported are with respect to the Reversible Hydrogen Electrode (RHE).

The ORR measurements were performed in 0.1 M $HClO_4$ solutions under flow of O_2 (research grade) using the glassy carbon rotating disk electrode (RDE) at a rotation rate of 1600 rpm and a sweep rate of 10 mV s^{-1}. In order to produce a clean electrode surface, several potential sweeps between 0.05 and 1.1 V versus RHE were applied to the electrode prior to the ORR measurement. In the ORR polarization curve, current densities were normalized in reference to the geometric area of the glassy carbon RDE (0.196 cm^2).

For the ORR at a RDE, the Koutecky-Levich equation can be described as follows:

$$1 / i = 1 / i_k + 1 / i_{l,c} = 1 / i_k + 1 / (0.62nFAD_0^{2/3}\omega^{1/2}\nu^{-1/6}C_0^{*}) \text{ --- } (1)$$

where i is the experimentally measured current, $i_{l,c}$ is the diffusion-limiting current, and i_k is the kinetic current; where D_0 is the diffusivity of oxygen in 0.1 M $HClO_4$ (estimated from the product of O_2 diffusivity at infinite dilution and the ratio of the dynamic viscosities of the electrolyte and pure water), n is the number of electrons in the O_2 reduction reaction (*i.e.*, $n = 4$), ν is the kinematic viscosity of the electrolyte, c_0 is the solubility of O_2 in 0. 1 M $HClO_4$, and ω is the rotation rate. Then, the kinetic current was calculated based on the following equation:

$$i_k = (i \times i_{l,c}) / (i_{l,c} - i) \text{ --- } (2)$$

For each catalyst, the kinetic current was normalized to the real surface area (0.2 cm^2). The accelerated durability tests were performed at room temperature in O_2 saturated 0.1 M $HClO_4$ solutions by applying cyclic potential sweeps between 0.6 and 1.1 V versus RHE at a sweep rate of 50 mV s^{-1} for a given number of cycles.

5. Synchrotron X-ray diffraction

X-ray diffraction (XRD) data were measured at 8C2 high-resolution powder diffraction beamline of Pohang Accelerator Laboratory (PAL). For the XRD, The incident X-rays were vertically collimated by a mirror, and monochromatized to the wavelength of 1.5490 Å using a double-crystal Si(111) monochromator. The detector arm of the vertical scan diffractometer is composed of seven sets of soller slits, flat Ge(111) crystal analyzers, anti-scatter baffles, and scintillation detectors, with each set separated by 20°. Each specimen was prepared by flat plate side loading method to avoid preferred orientation, and the sample was then rotated about the normal to the surface during the measurement in order to increase sampling statistics. Step scan was performed at room temperature from 20° in 2θ with 0.02° increment and 1° overlaps to the next detector bank up to 80° in 2θ.

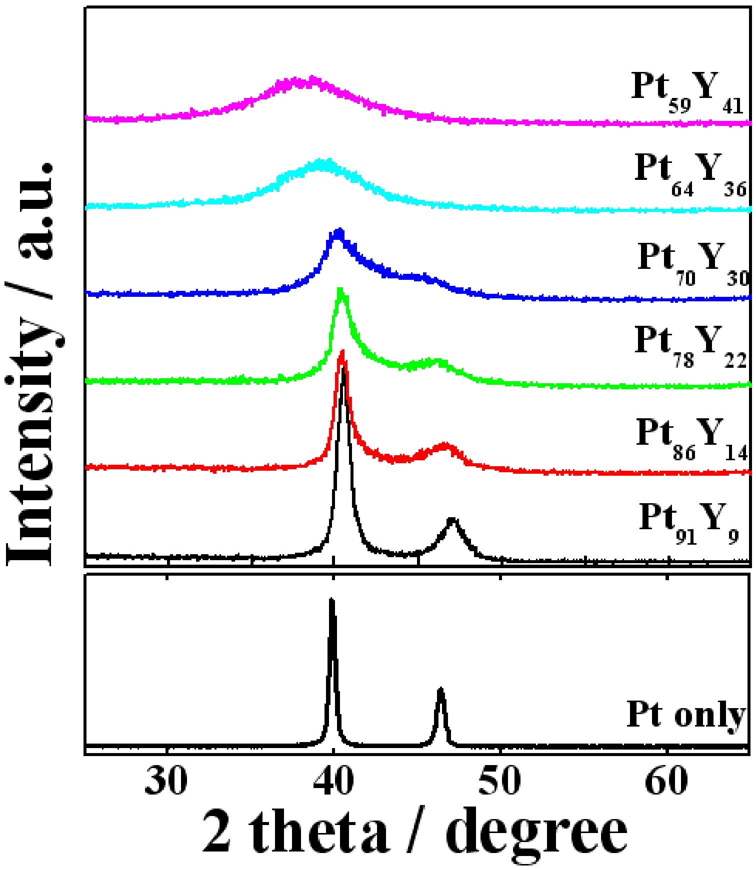

Figure S5. *X-ray diffraction patterns of the Pt and Pt-Y alloy catalysts studied in this work.*

6. Synchrotron high-resolution X-ray photoelectron spectroscopy

High-resolution X-ray photoelectron spectroscopy (HR-XPS) measurements were performed on the soft X-ray beamline (8A1) connected to an undulator (U7) at the Pohang Accelerator Laboratory (PAL). The end station was composed of a high performance electron analyzer (SCIENTA-200) with energy and angular resolution of 5 meV and 0.5°, respectively. The experiment was carried out in an ultrahigh vacuum (UHV) chamber with a base pressure $\leq 5 \times 10^{-10}$ Torr. All spectra were measured using 630 eV of incident photon energy. The Shirley background is subtracted from the measured spectra. The position of the center of the valence band is given by $\int N(\varepsilon)\varepsilon \, \mathrm{d}\varepsilon / \int N(\varepsilon) \, \mathrm{d}\varepsilon$, where $N(\varepsilon)$ is the DOS or, in our case, the XPS-intensity after background subtraction [3],[4]. The background-subtracted spectra were integrated up to 10.0 eV BE with respect to E_F, which is calculated from the Au film as a reference. Figure S5 shows the HR-XPS valence band (d-band) spectra from the Pt-Y and only Pt electrode samples. The observed valence band spectra of the surface of Pt-Y alloy catalysts clearly revealed a reduction in the density of states near the Fermi level as increasing of Y in Pt-Y alloy and shifting of the *d*-band center to higher binding energy. As shown in Figure S6, comparison of the *d*-band center of Y and Pt reveals a rough linear relation between them, as a function of the Y percentage. Mun et al. reported a trend in the *d*-band center shift with changing of Pd-Re surface composition [5]. Clearly, the direction of the *d*-band shift is consistent with Pd-Re surface composition.

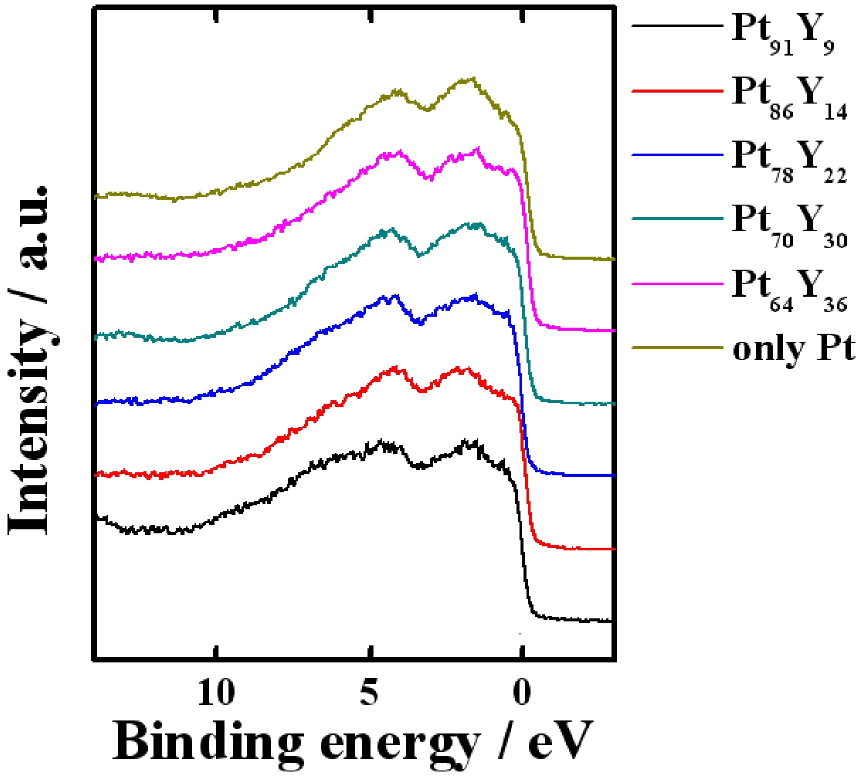

Figure S6. *Representative valance band spectra for Pt-Y alloy catalysts.*

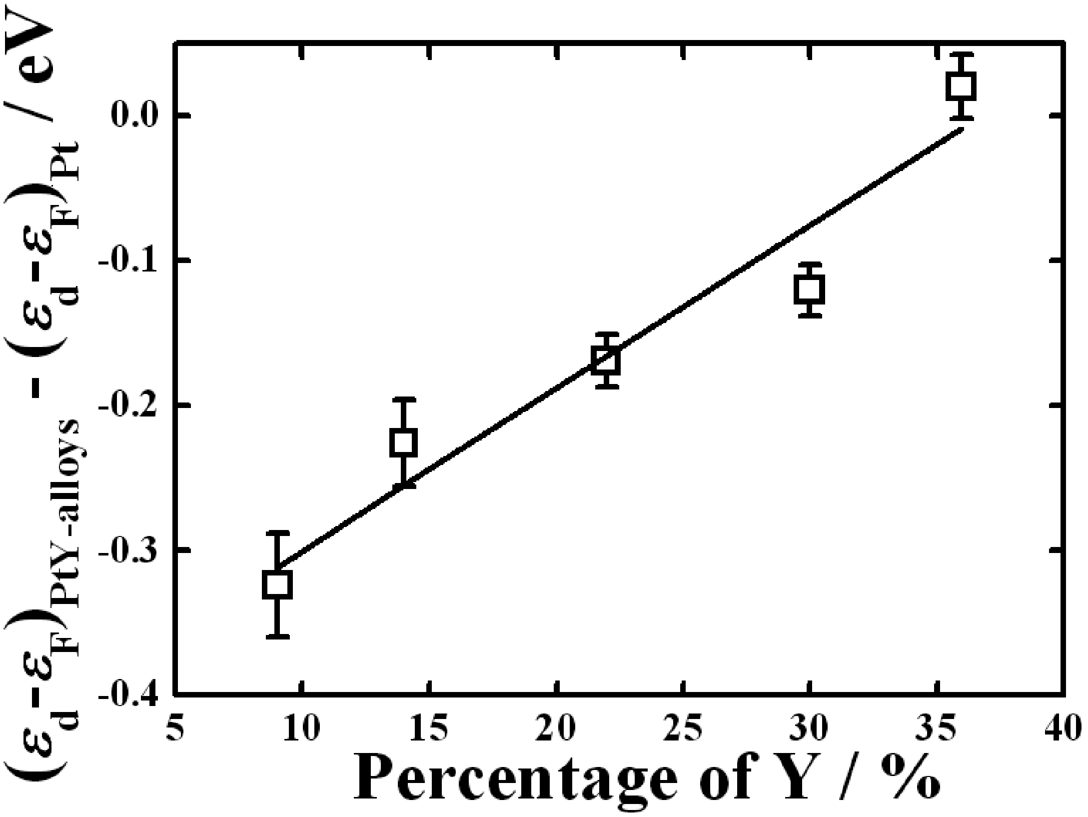

Figure S7. *Linear relationship between the d-band center and the percentage of Y.*

7. Synchrotron X-ray absorption spectroscopy

To evaluate this argument, we measured X-ray absorption near-edge spectroscopy (XANES) on Pt–Y alloys, and we measured the Pt L_{III} and L_{II} edges. One significant aspect of the XANES analysis is that it can provide important information on the Pt *d*-band vacancy. The *d*-band vacancy is derived from the analysis of the Pt L_{III} and L_{II} white lines. The L_{II} and L_{III} edges are due to the excitation of the $2p_{1/2}$ and $2p_{3/2}$ electrons, respectively. These electrons can undergo transitions to empty states in the vicinity of the Fermi level. Since the dipole selection rules in the XANES region restrict the transitions to L = 1 and J = 0, 1 (where L and J are the orbital angular quantum number and the total angular quantum number, respectively), the transitions to the *d*-orbitals are strongly favored [6]. In the case of Pt, it has been shown that the contribution of the final states with J = 5/2 is 14 times more than the contribution with J = 3/2. The L_{III} transition ($2p_{3/2}$ to $5d_{5/2}$) is thus more highly favored by the selection rules than the L_{II} transition ($2p_{3/2}$ to $5d_{5/2}$) [7]. The intensity of the L_{III} peaks, and to a lesser extent the L_{II} peaks, increases with increasing Pt *d*-band vacancy. X-ray absorption near edge structure (XANES) experiments were conducted on 5A beamline of Pohang Accelerator Laboratory (PAL) (2.5 GeV; 150-180 mA). The incident beam was monochromatized using a Si(111) double crystal monochromator and detuned by 30 % to minimize the contamination from higher harmonics, in particular, the third order reflection of the silicon crystals. The spectra for L_{III}-edge of Pt (E_0 =11564 eV) were taken in a transmission mode with separate He-filled IC Spec ionization chambers for incident and transmitted beams, respectively. Before measuring samples, energy was calibrated by using of Pt foil. The energy scan was performed in five regions for good energy resolution in a steep absorption and measurement of XANES spectra at a time, 5 eV-step in region of 11364-11514 eV, 1 eV-step in 11514-11554 eV, 0.25 eV-step in 11554-11594 eV, 0.03 *k*-step in 11594-12104 eV, and 0.04 *k*-step in 12104-12564 eV. Pre-edge absorption due to the background and detector were subtracted using a linear fit to the data in the range of -200 to -60 eV relative to E_0. E_0 was defined as the first inflection point on the rising absorption edge. Each spectrum was then normalized by a constant, extrapolated value to E_0 of third-order polynomial fit over absorption at 150-900 eV relative to E_0. The data analysis package used for XANES was the University of Washington's data analysis program. The XANES spectra were first subjected to background removal by fitting the pre-edge data to a Victoreen type formula over the range of 200 to 80 eV below the edge, followed by extrapolation over the energy range of interest and subtraction from the data. After the removal of the background contributions, the spectra were corrected for edge-shifts using the second derivatives of the inflection points of the data from the reference channel. The procedures used for normalization were the conventional ones. The normalization value was chosen as the absorbance at the inflection point of one EXAFS oscillation. The spectra were thus normalized by dividing each datum point by the normalization value. The edge areas (A_{2s} and A_{3s}) were calculated by numerical integration using Simpson's rule. The spectral window for such an integration was -10 to 13 eV, relative to the absorption edge. All of the areas (A_2, A_3, A_{3r}, and A_{2r}) were normalized by the X-ray cross section at the edge-jump and the density of the absorbing material [8].

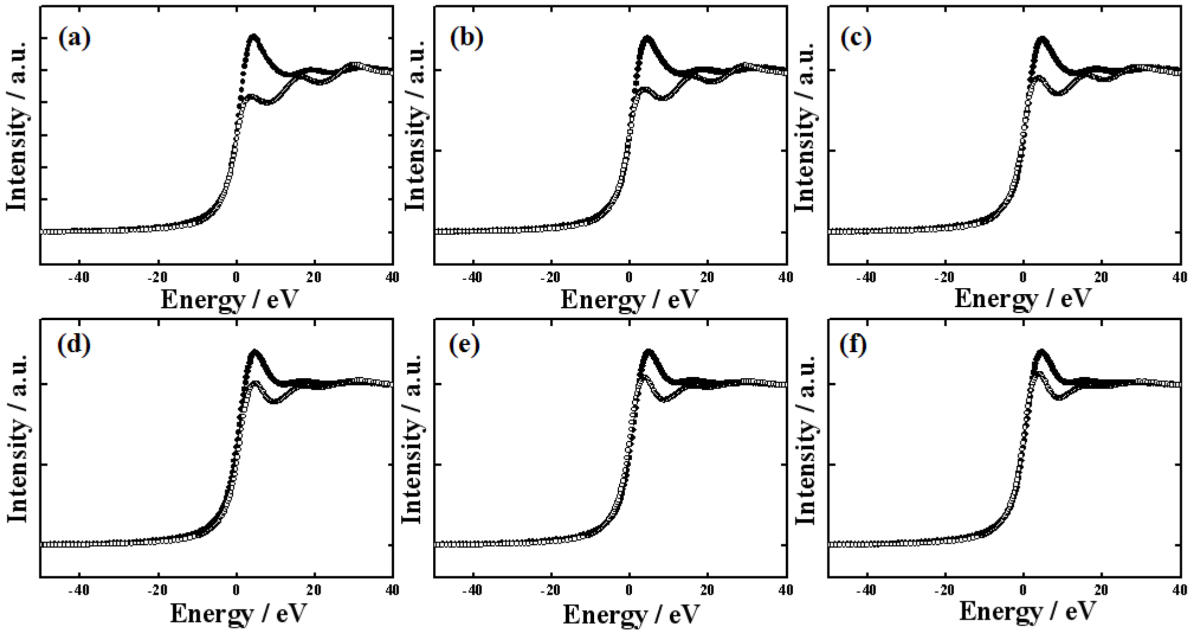

Figure S8. *XANES spectra of Pt-Y alloy catalysts. (a) $Pt_{91}Y_9$, (b) $Pt_{86}Y_{14}$, (c) $Pt_{78}Y_{22}$, (d) $Pt_{70}Y_{30}$, (e) $Pt_{64}Y_{36}$, and (f) $Pt_{59}Y_{41}$.*

8. Synchrotron extended X-ray absorption fine structure spectroscopy

The obtained data were processed in the usual way to obtain the absorbance and analyzed with ATHENA and ARTEMIS in the suite of IFEFFIT software programs [9]. To isolate EXAFS (extended X-ray absorption fine structure) signal, the post-edge background function was approximated with a piecewise spline that could be adjusted so that the low-R component of pre-Fourier transformed data were minimized. After calculation of EXAFS function $\chi(k)$, k^3-weighted EXAFS function in momentum (k) space was Fourier transformed to reveal the neighboring atoms arranged according to distance from a central As atom in R-space. The k range of the transform varied between a k_{min} of 2.0-3.0 Å^{-1} and a k_{max} of 12.0-13.0 Å^{-1}. Kaiser-Bessel function was adopted as a window function and the windowsill of dk=1.5 was also used in the transform. A shell of interest in R-space was back-transformed into the momentum space with Kaiser-Bessel window function and windowsill of dR=0.1. Fourier-filtered spectra derived from the experiments were fitted by using of the theoretical standards generated with the *ab-initio* FEFF 8.2 code [10]. The standard Pt-O and Pt-Pt phase-shift and amplitude functions were extracted from the structures of β-PtO_2 [11] and Pt metal [12], respectively.

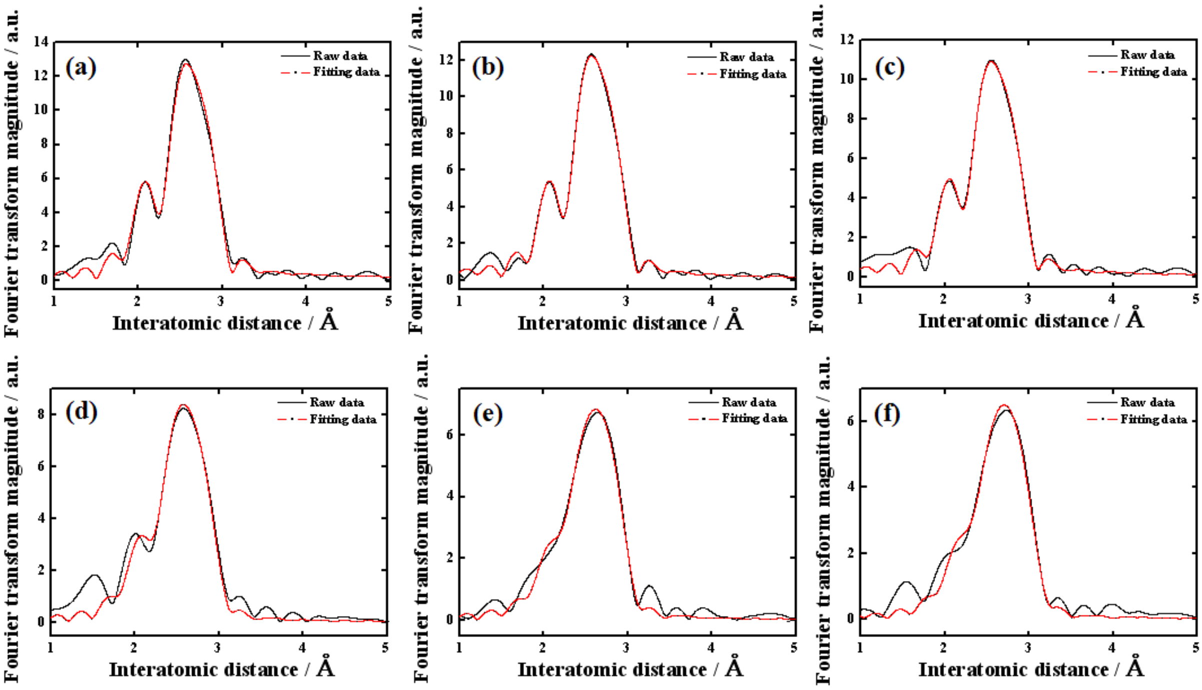

Figure S9. *EXAFS of Pt-Y alloy catalysts. (a) $Pt_{91}Y_9$, (b) $Pt_{86}Y_{14}$, (c) $Pt_{78}Y_{22}$, (d) $Pt_{70}Y_{30}$, (e) $Pt_{64}Y_{36}$, and (f) $Pt_{59}Y_{41}$.*

9. Computation method using DFT calculation

For both Pt(111) and $Pt_3Y(111)$ systems, all the calculations were carried out based on DFT, using the Vienna Ab-initio Simulation Package (VASP) [13,14]. A hexagonal 4×4 slab with five layers were generated as the substrate and a vacuum layer of 15 Å was added on the slab to simulate the surfaces within the periodic boundary condition. The top three layers were allowed to fully relax while the atoms in the fourth layer were only vertically relaxed. All the adatoms were set free so they can fully relax.

The relaxations of the electrons were described by projector augmented wave (PAW) potentials [15,16] with the exchange-correlation energy of the Perdew–Burke–Ernzerhof (PBE) parameterization [17,18] within the generalized gradient approximation (GGA). An energy cutoff of 400 eV and the gamma-centered Monkhorst-Pack scheme [19] were used to generate a 4×4×1 k-point mesh until the total energy difference of the system between the consecutive iterating steps became less than 10^{-4} eV. The geometric structure was optimized by the quasi-Newton or conjugate gradient techniques until the Hellmann-Feynman forces were below 0.02 $eVÅ^{-1}$. Spin polarization and dipole correction were not considered in this study except the cases for individual atoms, because several selected runs showed that they do not contribute any significant difference in the calculation results.

The adsorption energies of each adatom, E_{ad}^{adatom}, were calculated using the following equation:

$$E_{ad}^{adatom} = -[E_{slab}^{adatom} - (E_{slab} + E_{atom})] \tag{1}$$

where, E_{slab}^{adatom}, E_{slab}, and E_{atom} are the energy of slab with an adatom, that of the slab, and that of an isolated adatom, respectively. The positive adsorption energy indicates that the adsorption will occur spontaneously, while the negative adsorption energy indicates that the adsorption process is not energetically favorable.

The formation energy of the mono-vacancy, E_v was calculated using the following equation:

$$E_v = (E_{system-v}^{slab} + E_{atom}^{bulk}) - E_{system}^{slab} \tag{2}$$

where, $E^{slab}_{system-v}$, E^{bulk}_{atom}, and E^{slab}_{system} are the energy of the slab system with one vacancy, that of the constituting atom in bulk, and that of the slab system, respectively.

Table S2. *Cohesive energy of Pt and Y on Pt_3Y slab.*

	(a) Pure Pt	**(b) Pure Y**	**(c) Pt_3Y**
E_{coh} (eV / atom)	**5.53**	**4.39**	**6.23**

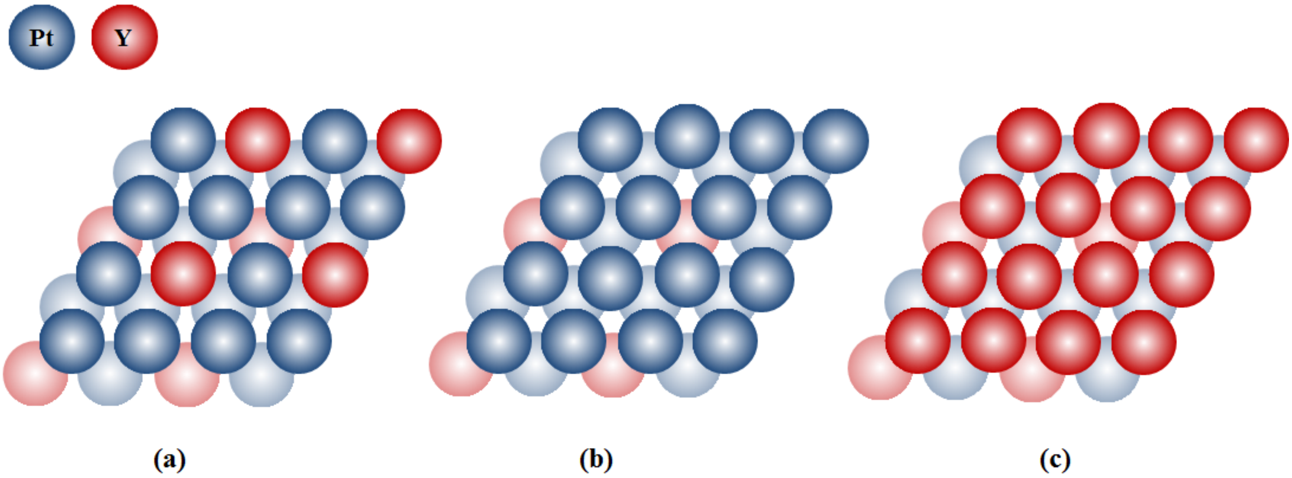

Figure S10. *Schematic diagrams of (a)* Pt_3Y*, (b) surface-all-Pt, and (c) surface-all-Y on* Pt_3Y *slab.*

Table S3. *Surface segregation of (a) Pt_3Y, (b) surface-all-Pt, and (c) surface-all-Y on Pt_3Y slab.*

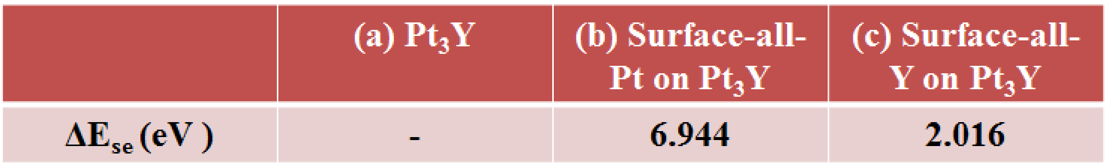

	(a) Pt_3Y	(b) Surface-all-Pt on Pt_3Y	(c) Surface-all-Y on Pt_3Y
ΔE_{se} (eV)	**-**	**6.944**	**2.016**

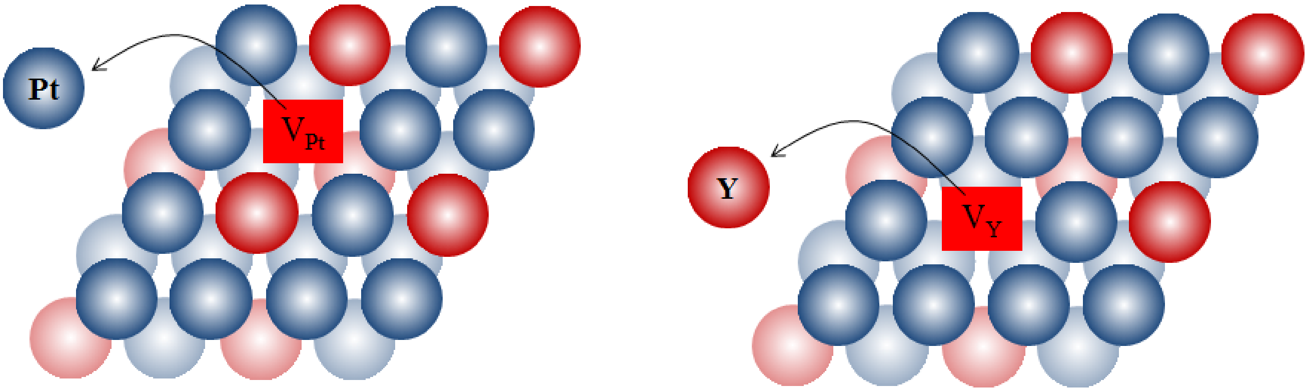

Figure S11. *Schematic diagram of (a) Pt and (b) Y dissociation on* Pt_3Y *slab.*

Table S4. *Dissociation energy of Pt and Y on Pt_3Y slab.*

	Pt on Pt_3Y	Pt on pure Pt	Y on Pt_3Y	Y on pure Y
E_d (eV /atom)	6.687	6.710	8.951	5.100

10. Fuel cell test of the Pt-Y alloy electrocatalysts fabricated by using sputter technique

Performance of polymer exchange membrane fuel cells (PEMFCs) that used the sputtered Pt, Pd, and Pt-Y catalysts was evaluated by measuring cell voltage of a 5-cm^2 cross-section of the catalyst zone under constant current conditions with a potentiometer. The commercial catalyst ink was prepared from a mixture of Pt/C (40 wt.%, Johnson Matthey (JM)) powder, isopropyl alcohol, Nafion solution (5 wt.%, Dupont) and de-ionized water. The single cell consisted of two graphite plates with serpentine flow-fields and two metal end-plates adjacent to the graphite plates. The MEA fabricated in this study was formed using Nafion 112 as the polymer electrolyte membrane. Before use, Nafion 112 was pretreated in a hydrogen peroxide solution (3 wt.%) for about 1 hr at 100 °C followed by washing in deionized water for 1 hr. The procedure described above was repeated, and the membrane then was boiled in a sulfuric acid solution (0.5 M) for 1 hr and washed in boiling de-ionized water for 1 hr. The prepared GDL and MEA were placed between two graphite plates, which then were assembled using the appropriate pressure. For the performance measurements, a humidified hydrogen and oxygen, at stoichiometric ratio of 1.5 : 2, was fed to the anode and cathode side of the single cell at a temperature of 75 / 70 ℃. During the measurement, the temperature was maintained at 70 °C and the pressure was held constant at atmospheric pressure. The cell voltage of each sample was obtained with increasing current density using a fuel cell test station (FCTS, Won-a tech) to measure the current-voltage curves.

Based this sputtering new technique, we carried out the electrochemical performances of PEMFCs single cells of $Pt_{70}Y_{30}$, pure Pt, pure Y electrocatalyst. In the previous paper, we reported that the fuel cell performance of Pt catalyst fabricated by using a high pressure (> 200 mTorr) sputtering technique in a gaseous mixture of Ar and He were comparable to the performance characteristics of a commercial catalyst [20]. In all cases, the amounts of 40 wt.% Pt/C (JM) (0.3 mg/cm^2) were added to the cathode and the amounts of $Pt_{70}Y_{30}$ (0.06 mg/cm^2) were added to the anode. Fuel cell performance curves were measured after allowing for a steady reading at each point during the current scan, as controlled by the fuel cell test station. The open circuit voltage of all samples sputtered showed an open circuit voltage of 1.0 ~ 0.9 V, which is close to that of commercial Pt catalysts. The fuel cell performance of $Pt_{70}Y_{30}$ catalyst showed a maximum power density of the 4.82 $W/(mg \cdot cm^2)$, which is comparable to the 3.51 $W/(mg \cdot cm^2)$ for the Pt/C catalyst. In particular, at 0.6 V, the current density of $Pt_{70}Y_{30}$ catalyst is 1.5-fold more active than corresponding Pt/C catalyst. From a practical perspective, we show that it is possible to devise an ORR electrocatalyst.

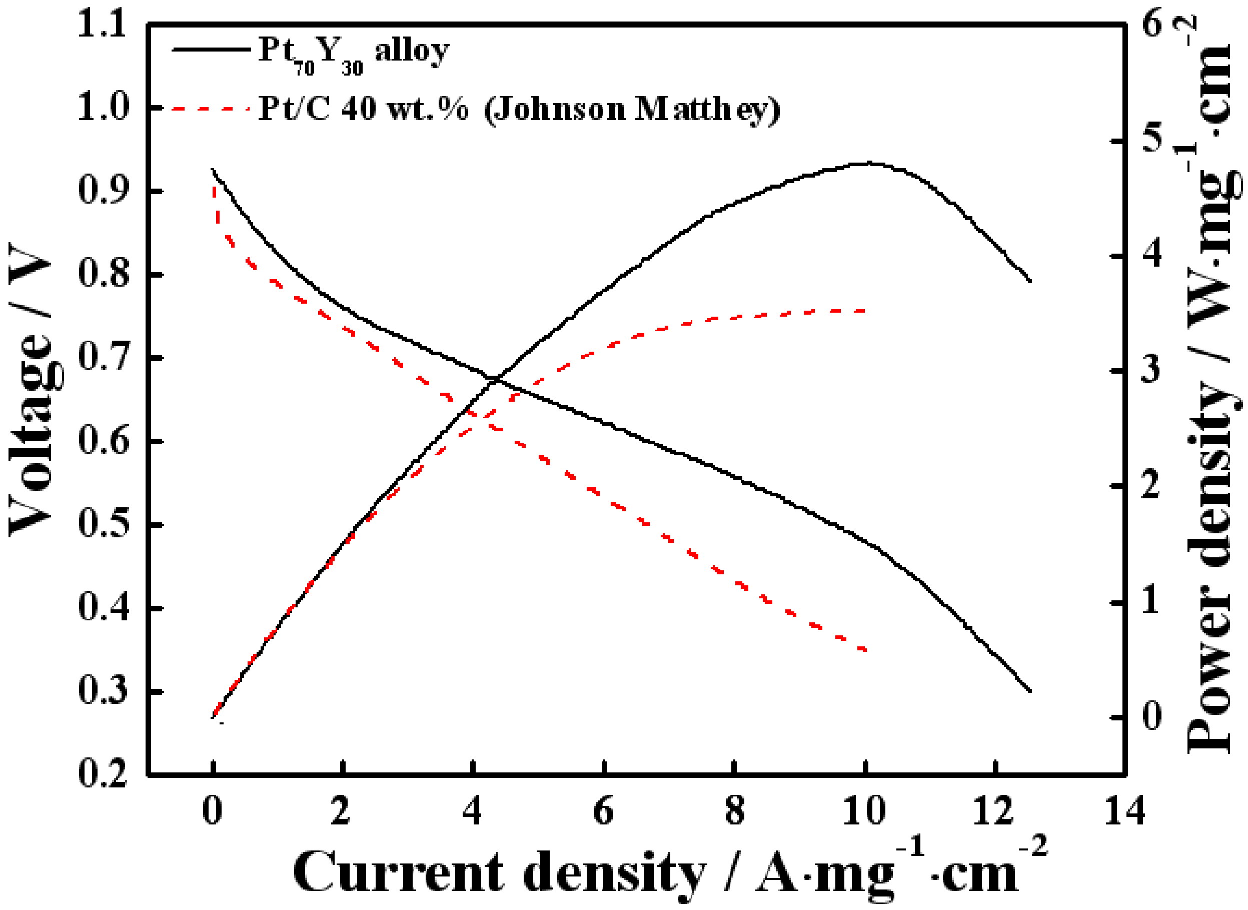

Figure S12. *Polarization curves and power density curves of MEAs with $Pt_{70}Y_{30}$ (—) formed at different sputtering pressures of 200 mTorr with a mixture of gaseous Ar and He mixture (Ar/He = 1) and Pt/C 40wt.% (JM) (---).*

11. Y 3d peaks using synchrotron high-resolution X-ray photoelectron spectroscopy

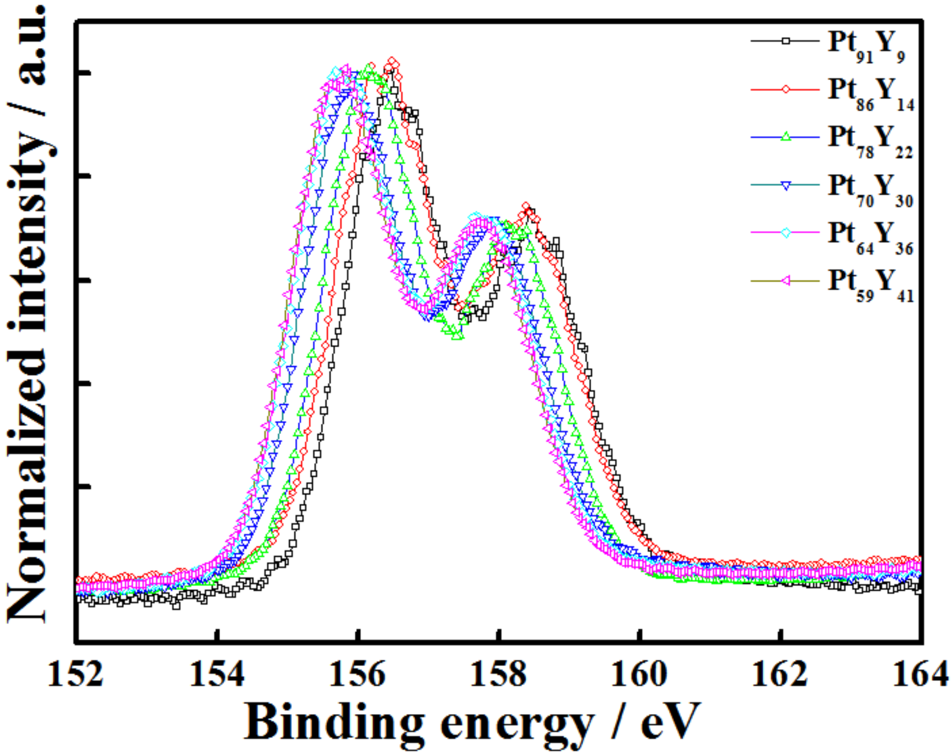

Figure S13. *Y 3d peaks of Pt-Y alloy catalysts.*

12. References

[1] E. Gagaoudakis, M. Bender, E. Douloufakis, N. Katsarakis, E. Natsakou, V. Cimalla,G. Kiriakidis, *Sensor. Actuators B* **2001**, *80*, 157.

[2] K. Y. Chan, T. Y. Tou, B. S. Teo, *Microelectron. J.* **2006**, *37*, 608.

[3] W. P. Zhou, A. Lewera, R. Larsen, R. L. Masel, P. S. Bagus, A. Wieckowski, A. *J. Phys. Chem. B* **2006**, *110*, 13393.

[4] V. R. Stamenkovic, B. Fowler, B. S. Mun, G. F. Wang, P. N. Ross, C. A. Lucas, N. M. Markovic, *Science* **2007**, *315*, 493.

[5] B. S. Mun, C. Lee, V. Stamenkovic, N. M. Marković, P. N. Ross, *Phys. Rev. B* **2005**, *71*, 115420.

[6] L. M. Falicov, W. Hanke, M. P. Maple, *Valence Fluctuation in Solids*, Nprth-Holland Pub., Amsterdam, **1981**.

[7] A. E. Russell, S. Maniguet, R. J. Mathew, J. Yao, M. A. Roberts, D. Thompsett, *J. Power Sources* **2001**, *96*, 226-232.

[8] A. N. Mansour, J. W. Cook, D. E. Sayers, *J. Phys. Chem.* **1984**, *88*, 2330.

[9] B. Ravel, M. Newville, *J. Synchrotron. Radiat.* **2005**, *12*, 537.

[10] A. L. Ankudinov, B. Ravel, J. J. Rehr, S. D. Conradson, *Phys. Rev. B* **1998**, *58*, 7565.

[11] S. Siegel, R. H. Henry, S. T. Benjamin, *J. Inorg. Nucl. Chem.* **1969**, *31*, 3803.

[12] J. S. Kasper, K. Lonsdale, International Tables for X-ray Crystallography. V.3. D. Reidel Pub. Co., **1985**.

[13] G. Kresse and D. Joubert, *Phys. Rev. B.* **1999**, *59*, 1758.

[14] http://cms.mpi.univie.ac.at/vasp, **2010**.

[15] G. Kresse and J. Furthmüller, *Comp. Mater. Sci.* **1996**, *6*, 15.

[16] P. E. Blöchl, *Phys. Rev. B.* **1994**, 50, 17953.

[17] J. P. Perdew, K. Burke, and M. Ernzerhof, *Phys. Rev. Lett.* **1996**, *77*, 3865.

[18] B. Hammer, L. B. Hansen and J. K. Nørskov, *Phys. Rev. B.* **1999**, *59*, 7413.

[19] H. J. Monkhorst and J. D. Pack, *Phys. Rev. B.* **1976**, *13*, 5188.

[20] S. J. Yoo, Y.-H. Cho, Y.-H. Cho, H.-S. Park, J. K. Lee, Y.-E. Sung. *J. Power Source* **2008**, *178*, 547.